International Symposium
On Turbulence and Shear Flow
Phenomena (TSFP-9)
June 30 - July 3, 2015 *Melbourne, Australia*

WAVE-LENGTH-DEPENDENT REARRANGEMENT OF SECONDARY VORTICES OVER SUPERHYDROPHOBIC SURFACES WITH STREAMWISE GROOVES

A. Stroh[1], Y. Hasegawa[2], J. Kriegseis[1] and B. Frohnapfel[1]

[1] Institute of Fluid Mechanics,
Karlsruhe Institute of Technology,
Karlsruhe, Germany
alexander.stroh / jochen.kriegseis / bettina.frohnapfel @kit.edu

[2] Institute of Industrial Science,
The University of Tokyo,
Tokyo, Japan
ysk@iis.u-tokyo.ac.jp

ABSTRACT

An investigation of the flow dynamics over a superhydrophobic surface (SHS) carrying streamwise micro grooves is performed in a fully developed turbulent channel flow under a constant pressure gradient (CPG). The SHS is modeled as a flat boundary with alternating no-slip and slip conditions. A series of direct numerical simulations (DNS) is carried out systematically varying the spanwise periodicity of the streamwise grooves. It is observed that the alternating no-slip and free-slip boundary conditions cause a spanwise inhomogeneity of the Reynolds shear stress near the SHS, and consequently generate Prandtl's second kind of secondary flow characterized by coherent streamwise vortices. The arrangement and rotational direction of these motions are shown to be strongly affected by the dimension of the introduced SHS. Therefore, the detailed turbulent statistics are obtained and the effect of the secondary flow on the resultant flow rate increase is discussed. For the clarification of the secondary flow nature, the vortical structures are investigated by means of streamline-based topology analysis and complementary application of the vorticity transport equation.

INTRODUCTION

The reduction of skin friction drag in turbulent flows is an important issue linked to the efficient use of available energy resources. Superhydrophobic surfaces are shown to be an interesting approach to this issue in water flows. These surfaces are able to enforce local free-slip-like conditions at the wall due to the coating with a certain roughness pattern, which entraps air in the surface cavities. Since the shear stress at a liquid-gas interface is much lower than the stress at a fully wetted liquid-solid interface, the overall skin friction drag is significantly reduced.

The effects of SHS in the laminar flow regime have been analytically analyzed by Philip (1972), while investigations in the turbulent regime have been conducted only in the last decade by means of experiments (Daniello *et al.*, 2009) and numerical simulations (Min & Kim, 2004; Martell *et al.*, 2009). The recent work by Türk *et al.* (2014) states a possible flow rate increase up to 50% under constant pressure gradient conditions in a fully developed turbulent channel flow with SHS in comparison to plain channel flow and proposes a model for SHS simulations based on an eddy viscosity approach. This work also shows the appearance of secondary motions over SHS due to the spanwise inhomogeneity of the boundary conditions at the wall.

The results of Türk *et al.* (2014) show an opposite rotational direction of the induced vortical motions when the spanwise extent of the surface grooves, L, as depicted in Figure 1 is increased from 140 to 280. This change of the rotational direction is found to affect the resultant drag reduction effect. In their study, the authors hypothesize that this change occurs due to the absence of direct interaction between the small-scale secondary motions at the no-slip/free-slip interface for larger L. Instead, large-scale tertiary motions are introduced by a pair of secondary vortices. In order to further investigate this hypothesis we focus on the analysis of the SHS-induced secondary motions in dependence of the no-slip/free-slip area size for $140 < L < 280$, where the switch of the secondary motion rotation occurs. It should be noted that the present study assumes the existence of a stable and flat liquid-gas interface. This model assumption is probably limited to small values of L (Seo *et al.*, 2013; Türk *et al.*, 2014). Nevertheless, similar phenomenon for secondary motion is also observed in the work of Goldstein & Tuan (1998) where a cross-plane secondary motion appears in turbulent flow over streamwise oriented riblets if a certain riblet spacing is exceeded.

PROCEDURE

A series of DNS has been carried out in a fully turbulent channel flow driven by a CPG. For an incompressible Newtonian fluid, the flow satisfies the continuity and Navier-Stokes equations:

$$\frac{\partial u_i^*}{\partial x_i^*} = 0, \tag{1}$$

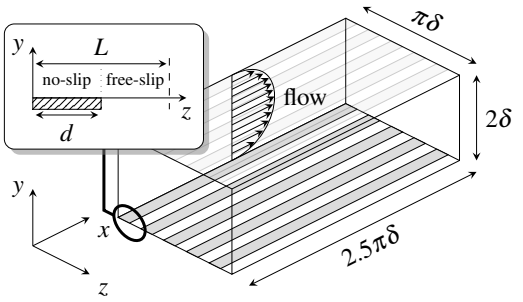

Figure 1. Schematic of the numerical domain with no-slip / free-slip boundary conditions at the walls.

$$\frac{Du_i^*}{Dt^*} = -\frac{1}{\rho^*}\frac{\partial p^*}{\partial x_i^*} + \nu^* \frac{\partial^2 u_i^*}{\partial x_j^* \partial x_j^*}, \tag{2}$$

where p^* is the static pressure and ν^* is the kinematic viscosity. The asterisk denotes a dimensional quantity, while otherwise quantities are non-dimensionalized by the friction velocity, $u_\tau^* = \sqrt{\tau_w^*/\rho^*}$, such that $u = u^*/u_\tau^*$, $x_i = x_i^* u_\tau^*/\nu^*$ and $t = t^* u_\tau^{*2}/\nu^*$ (viscous units). Note that u_τ^* remains unchanged across the investigated parameter range, since the pressure gradient is kept constant during the simulation. The same applies for the friction Reynolds number given by $\mathrm{Re}_\tau = u_\tau^* \delta^*/\nu^* = 180$ where δ^* is the half channel height.

The Navier-Stokes equations are numerically integrated by a finite difference method on a staggered grid with a fractional step method for pressure decoupling. For temporal advancement, the convection and viscous terms are discretized using the 2nd order Adams-Bashforth and Crank-Nicholson methods, respectively. The schematic of the numerical domain is depicted in Figure 1. Periodic boundary conditions are applied in streamwise (x) and spanwise (z) directions, while the wall-normal (y) extension of the domain is bounded by alternating no-slip / free-slip boundary conditions at the upper ($y = 2\delta$) and lower wall ($y = 0$). An impermeability condition is applied for the wall-normal velocity component on the entire area of both channel walls. The wave-length, L, represents the size of the alternating structure with a solid fraction $\Phi = d/L = 0.5$. The secondary motion is observed in the cross sectional plane perpendicular to the main flow direction. For the variation of L the number of grid nodes in spanwise direction is adjusted, while the spanwise resolution, Δz and, is kept constant. Consequently, the spanwise extension of computational domain varies with L and the wall area is always covered by four wave-lengths (Table 1). Since the change of the secondary flow rotation occurs in the range $140 < L < 280$, following wave-lengths are selected for simulations: $L = 108$, 126, 144, 148, 153, 158, 162, 171, 180, 202, 225 and 252. Additionally, the data-sets from Türk *et al.* (2014) for $L = 35.2, 70.8, 141.4$ and $L = 282.8$ with $\Delta z = 2.209$ are used in the present investigation.

Table 1. Numerical properties of the performed DNS.

$N_x \times N_y \times N_z$	$x \times y \times z$	Δx	$\Delta y_{\min}$	Δz
$128 \times 129 \times 128 - 512$	$1413 \times 360 \times 280 - 1152$	11	0.1	2.25

The statistical data-set is obtained for an integration time of approximately 200 eddy turn-overs. Considering the periodic nature of the streamwise grooves, we introduce the phase averaging operator as

$$\bar{\varphi}(\theta, y) = \frac{1}{N}\sum_{n=1}^{N} \int_t \int_x \varphi\left(x, y, L\left(\frac{\theta}{2\pi} + n\right), t\right) \mathrm{d}x\mathrm{d}t, \tag{3}$$

where φ is an arbitrary variable as a function of space and time, whilst θ is a phase with respect to the periodic structure and N is a number of periods in the computational domain. Hence, any flow quantity can be decomposed into the phase averaged and the random components:

$$\varphi(x, y, z, t) = \bar{\varphi}(\theta, y) + \varphi'(x, y, z, t). \tag{4}$$

In this paper, the secondary flow is regarded as the phase averaged flow field. Additionally, using an assumption of symmetrical velocity distribution with respect to the middle-line of the no-slip or the free-slip region as well as to the channel half-height, we perform corresponding spatial averaging in order to obtain smoother statistical data.

Flow field analysis based on topology considerations as comprehensively discussed e.g. by Foss (2004) is applied to the resultant vector fields in order to understand the arrangement of the appearing secondary motions. One such example of secondary flow is illustrated in Figure 2(a) for $L = 162$ and $\Phi = 0.5$. Line integral convolution (LIC, Cabral & Leedom (1993)) is used for the identification of the singular points in the vector field such as nodes (N), saddles (S) and half-saddles (S'). Finally, a topological map is derived from the position of the singular points and LIC (Figure 2(b)).

Considering velocity invariant methods, an analysis of the secondary flow dynamics based on the vorticity production terms is performed. Utilizing the definition for the streamwise vorticity

$$\bar{\omega}_x = \frac{\partial \bar{w}}{\partial y} - \frac{\partial \bar{v}}{\partial z}, \tag{5}$$

combined with the Navier-Stokes equations (2) for the wall-normal ($i = 2$) and spanwise ($i = 3$) velocity component we obtain the following transport equation for the phase averaged streamwise vorticity:

$$\bar{v}\frac{\partial \bar{\omega}_x}{\partial y} + \bar{w}\frac{\partial \bar{\omega}_x}{\partial z} = \underbrace{-\frac{\partial^2 \overline{v'w'}}{\partial y^2} - \frac{\partial^2 \overline{w'w'}}{\partial y \partial z} + \frac{\partial^2 \overline{v'v'}}{\partial y \partial z} + \frac{\partial^2 \overline{v'w'}}{\partial z^2}}_{\text{streamwise vorticity production, } P_{\bar{\omega}_x}} + \frac{1}{Re_\tau}\left(\frac{\partial^2 \bar{\omega}_x}{\partial y^2} + \frac{\partial^2 \bar{\omega}_x}{\partial z^2}\right). \tag{6}$$

The terms on the left-hand-side represent the convection of $\bar{\omega}_x$ due to the secondary flow. The first four terms on the right-hand-side are production terms of $\bar{\omega}_x$, while the last term represents the viscous diffusion of $\bar{\omega}_x$. Note that the production terms have non-zero values only when the no-slip and free-slip surfaces are resolved. Therefore, the effective slip models which are homogeneous in the spanwise direction (Min & Kim, 2004; Fukagata *et al.*, 2006) are not able to predict the formation of the secondary flow.

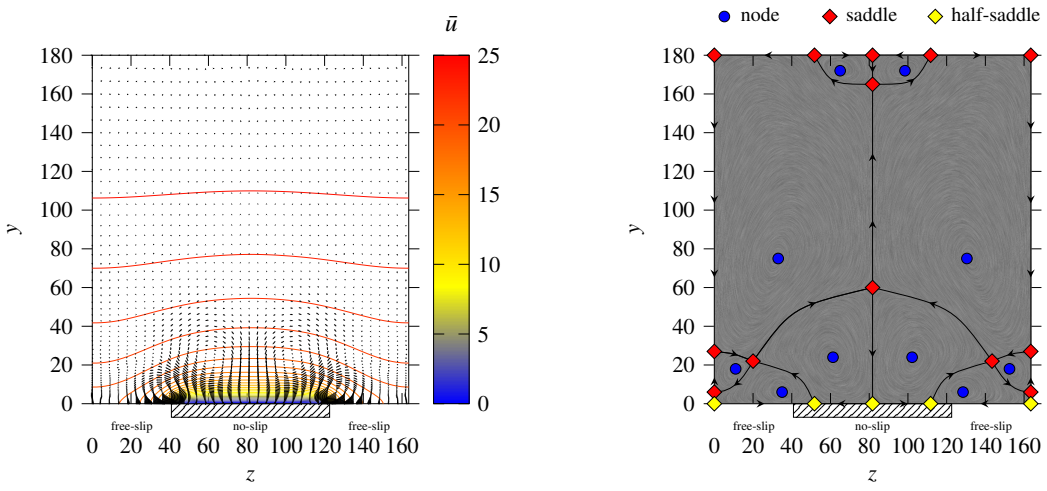

(a) vector plot with streamwise mean velocity

(b) topological map with LIC in background

Figure 2. Secondary motions over SHS in y-z-plane for $L = 162$ and $\Phi = 0.5$.

TOPOLOGICAL REARRANGEMENT

Figure 3 illustrates the change of the flow topology for increasing L by introducing color coding for the same vortical structures at different wave-lengths. The SHS with wave-lengths up to $L = 140$ show similar flow topology with two counter-rotating large-scale secondary vortices causing an upward motion above the no-slip area and a downward motion above the free-slip area. Starting from $L = 144$ the flow topology significantly changes, for $L = 149$ a formation of two additional vortices above the middle of the no-slip area and two arising vortices above the no-slip / free-slip edge can be clearly identified. Further increase of the wave-length to $L = 162$ demonstrates an even more complex topology map with an additional vortex-pair above the free-slip region. An expansion of the previously observed near-wall vortical structures above the no-slip region occurs, while the edge vortices grow and move towards the wall. The large-scale motions are pushed farther to the outer flow region. For $L = 171$ we see that the newly appeared vortex-pair is absorbed by the growing vortices above the no-slip region, while the vortex-pair which was dominant for smaller L is shrinking. Starting from $L = 180$ the size of the edge vortices is successively reduced and the vortices above the no-slip area dominate the cross section of the flow field. For $L = 202$ only two vortex-pairs can be observed - the small edge vortices which completely disappear for $L > 252$ and the major vortex-pair occupying the entire domain half-height. Comparing the topology map of the flow over SHS at $L = 141$ and $L = 202$ one can clearly see that the rotational direction of the dominating vortex-pair is reversed. For larger L, flow is pushed towards the wall above the no-slip region, while an upward motion occurs above the free-slip area. Hence, the switch of the rotation is a consequence of a complete reorganization of secondary motions caused by the increase of the wave-length.

It has to be emphasized that the strength of the observed motions varies depending on L. Figure 4(a) shows the maximum magnitude of the secondary motion normalized by the corresponding bulk mean velocity, U_b. For the cases up to $L = 108$ the magnitude of the secondary motion increases to 1% of the bulk mean velocity followed by a decrease of the magnitude between 126 and 180 where the rearrangement of vortical structures occurs. For the larger L with opposite rotational direction of the dominant structures the secondary motion strength increases again and reaches $1-2\%$ of U_b for $200 < L < 288$.

The influence of the secondary motion on the increase of bulk mean velocity is shown in Figure 4(b). The plot compares the present DNS results with a model prediction without secondary flow and with consideration of secondary motion, where $\bar{v}$ and $\bar{w}$ extracted from the DNS data is used for the evaluation of convective terms. The model utilizes a uniform y-dependent turbulent viscosity profile evaluated from the empirical relation by Reynolds & Hussain (1972) with adjustment of van Driest constant (Türk *et al.*, 2014). The model without secondary motion over-predicts the increase of U_b by $4-22\%$, while the overshoot increases for larger L. The model with secondary motion improves the prediction of U_b especially for larger L and cases where secondary motion intensity is significant (e.g. $L = 108$, Fig. 4(a)). When the secondary motion is taken into account the model over-prediction does not exceed 10% and remains $< 5\%$ for $L < 126$ and $L > 225$. The strongest deviation from the DNS data is observed for $126 < L < 225$ where the rearrangement of the secondary structures occurs.

In order to clarify the influence of the solid fraction on the secondary motion formation a parametric study with variation of Φ at constant $L = 162$ is performed. Figure 5 illustrates the change of the secondary motion topology when the solid fraction is slightly reduced or increased. It is evident that a slight reduction of the solid fraction at $L = 162$ ($\Phi = 0.43$ with $d = 70$) corresponding to an increase of the free-slip spacing leads to a simplification of the motion topology with two smaller-scale edge vortices and the larger-scale vortex-pair above. This configuration strongly resembles the topology present for $\Phi = 0.5$ and wave-length $L \geq 171$ (Figure 3). An increase of the solid fraction at $L = 162$ ($\Phi = 0.57$ with $d = 92$) also meaning a reduction of the free-slip spacing shows the opposite effect: the large-scale edge vortex-pair dominates the topology while the vortex-pair above the no-slip region is reduced in size. This topology is similar to the cases with $\Phi = 0.5$ at $L < 162$ (e.g. Figure 3, $L = 149$). The observation suggests that the secondary flow topology is rather determined by the dimension of the free-slip area while the influence of the no-slip spacing is minor.

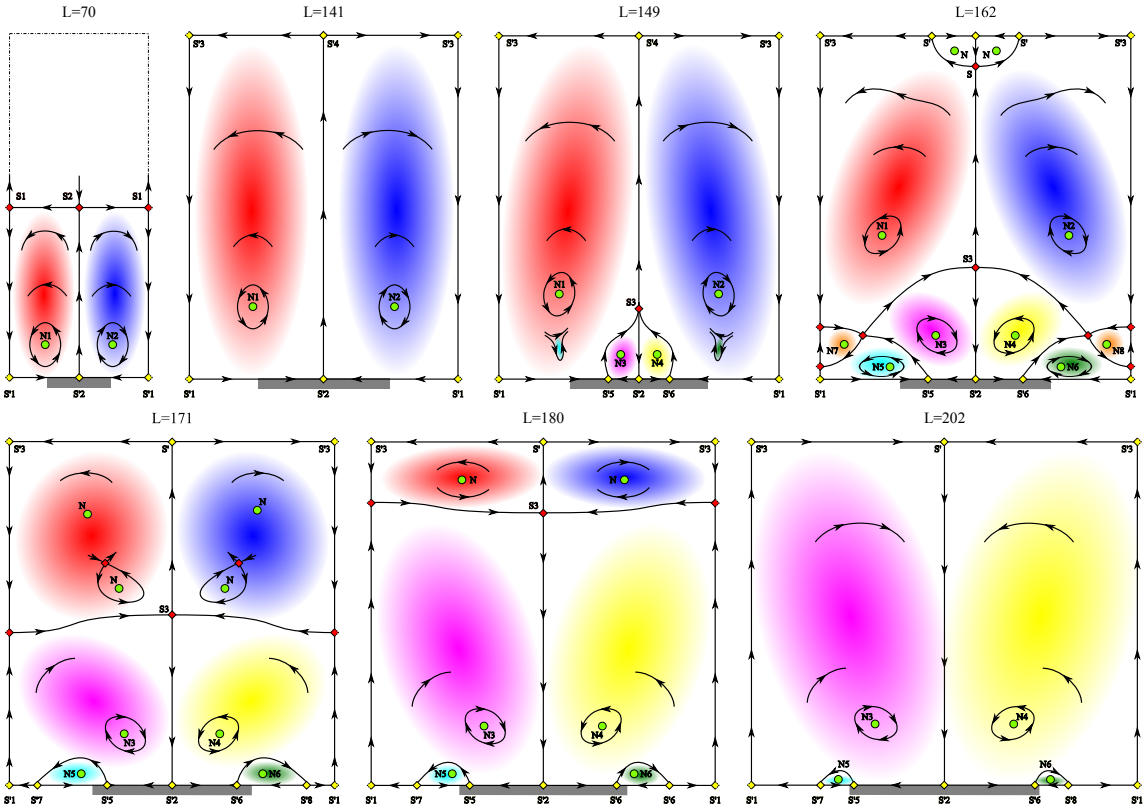

Figure 3. Topology map of the considered flow: spatial evolution of the singularities and vortical structures over SHS for increasing L with $\Phi = 0.5$. Color code marks the identical vortical structures.

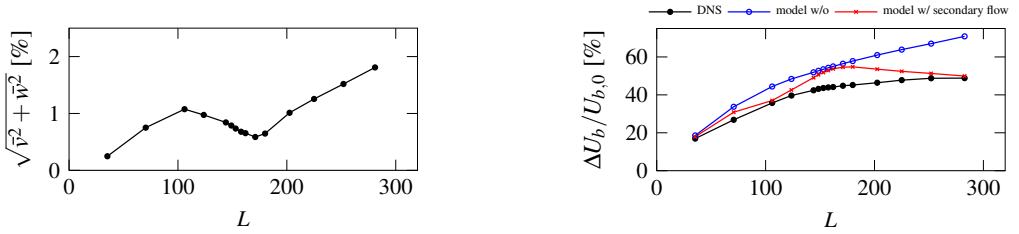

(a) maximum magnitude normalized by the U_b at $\Phi = 0.5$.

(b) flow rate increase due to SHS at $\Phi = 0.5$.

Figure 4. Properties of the secondary motions.

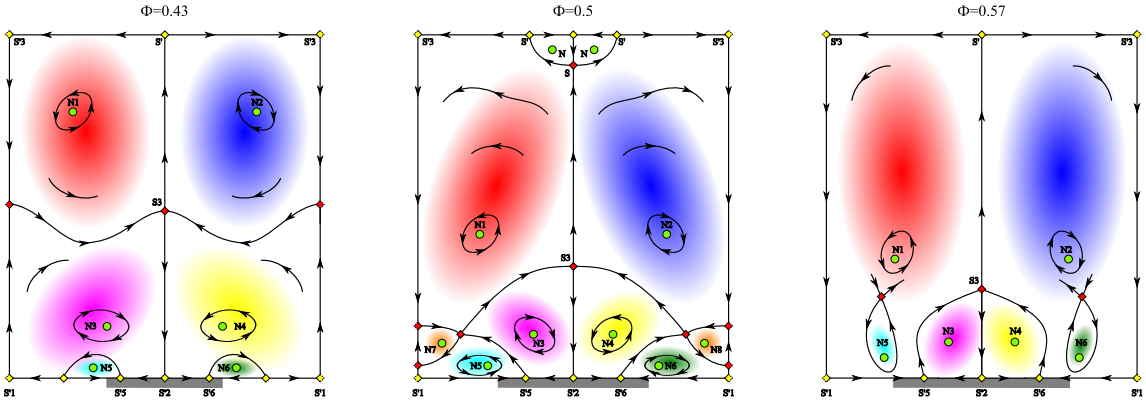

Figure 5. Topology map of the considered flow: spatial evolution of the singularities and vortical structures over SHS for changing Φ at $L = 162$. Color code marks the identical vortical structures.

VORTICITY ANALYSIS

Figure 6 shows the distribution of $\bar{\omega}_x$ in the vicinity of the wall for the wave-lengths $L = 108, 162$ and 225. Distribution of $\bar{\omega}_x$ agrees well with the location of the vortical structures presented previously in the topological map (Figure 3). Figure 7 presents the distribution of the total vorticity production, $P_{\bar{\omega}_x}$, from Equation (6) with the spanwise coordinate normalized by L (Fig. 7(a)) and the viscous units (Fig. 7(b)), whereas the wall-normal coordinate is normalized with viscous unit in both figures. In the latter plot we demonstrate only the left half of the periodic SHS ($z/L = 0 - 1/2$ in Fig. 7(a)) with horizontally aligned free-slip / no-slip edge for all L in order to enable easier comparison. The highest magnitude of the vorticity production can be observed around the no-slip / free-slip edges, confirming the fact that the secondary motions are inherently triggered by the alteration of the wall boundary condition, which translates into inhomogeneity of the Reynolds stress. Interestingly, the distribution of $S_{\omega,x}$ remains qualitatively and quantitatively very similar for all investigated L in spite of the obvious differences in distributions of vorticity and topology of the secondary flow. The wall-normal extent of the vorticity production spots is slightly dependent on L, reaching $y \approx 6 - 8$. Considering spanwise extent, a triangle-shaped distribution can be observed above the free-slip region, which seems to scale with L as suggested from Figure 7(a). The part of the distribution above the no-slip region rapidly vanishes within $z \approx 7 - 10$ from the free-slip / no-slip edge due to the presence of no-slip condition at the wall. Presumably, the wall-normal extent of the vorticity production distribution and its spanwise extent over the no-slip region decays within approximately $6 - 10$ viscous units from the free-slip / no-slip edge, while the spanwise extent of the distribution above free-slip area scales with the size of the free-slip region or L.

Figure 8 reveals a complex composition of the governing terms in the vorticity production from Equation (6) for $L = 162$. The main contribution to the total vorticity production arises from the first two terms of $S_{\omega,x}$, $-\frac{\partial^2 \overline{v'w'}}{\partial y^2}$ and $-\frac{\partial^2 \overline{w'w'}}{\partial y \partial z}$. These terms originate from the momentum equation for the spanwise velocity component. The contribution from the fourth term, $\frac{\partial^2 \overline{v'w'}}{\partial z^2}$, is rather minor, while the third term, $\frac{\partial^2 \overline{v'v'}}{\partial y \partial z}$, shows significantly smaller values than the governing terms and is therefore neglected. Latter terms originate from the momentum equation for the wall-normal velocity component. The fact that the vorticity production mainly emerges from the equation for the spanwise velocity component is reasonable due to the definition of the imposed boundary conditions: the introduction of SHS implies only changes of the boundary condition for the streamwise and spanwise component, while the impermeability in the wall-normal direction still holds at no-slip and free-slip regions.

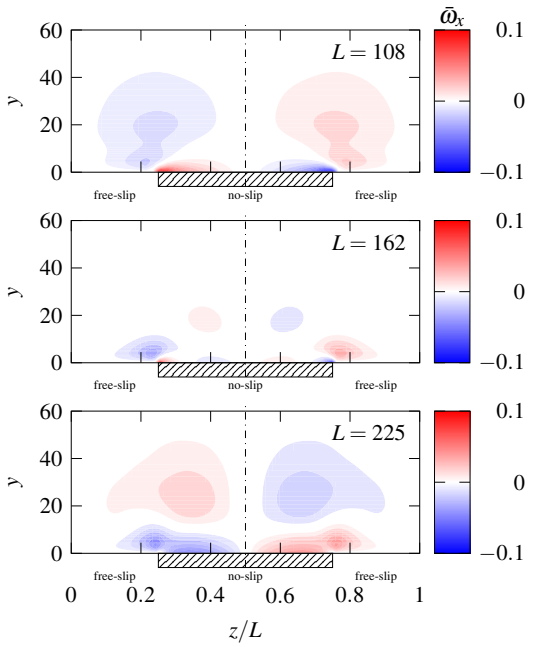

Figure 6. Vorticity distribution for for $L = 108, 162, 225$ and $\Phi = 0.5$.

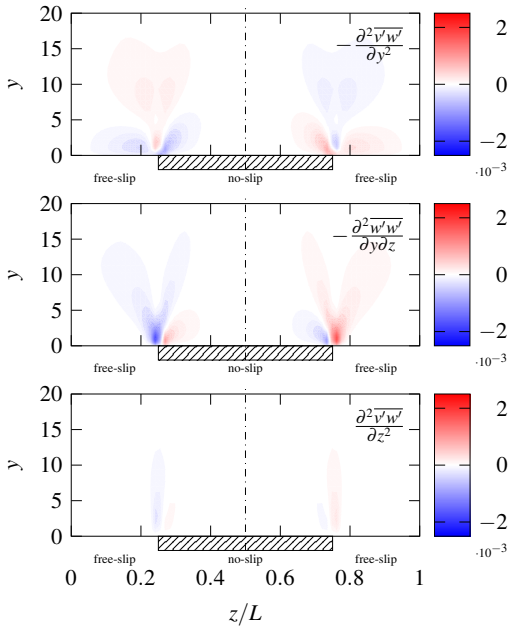

Figure 8. Governing terms of the vorticity production for $L = 162$ and $\Phi = 0.5$.

SUMMARY AND OUTLOOK

A detailed investigation of the statistical data of turbulent channel flow DNS with streamwise oriented SHS for $35 < L < 288$ reveals a series of significant changes in the structure of the occurring secondary motions leading to topological transition in this wave-length region. It is shown that secondary flow can account for up to 15% of $U_{b,0}$ for larger L and its consideration in modelling approach significantly improves prediction of U_b. The singular point analysis shows that the only counter-rotating vortex pair appearing for $L < 140$ is displaced by a complex entity of other structures for $144 < L < 202$ and then completely replaced by a different vortex pair with opposite rotational direction for $L \geq 202$. The analysis of the streamwise vorticity transport equation shows that the secondary flow is driven by the vorticity production distribution concentrated at the edge between free-slip and no-slip region, which originates from the switch of boundary conditions at the wall translated into the inhomogeneity of Reynolds

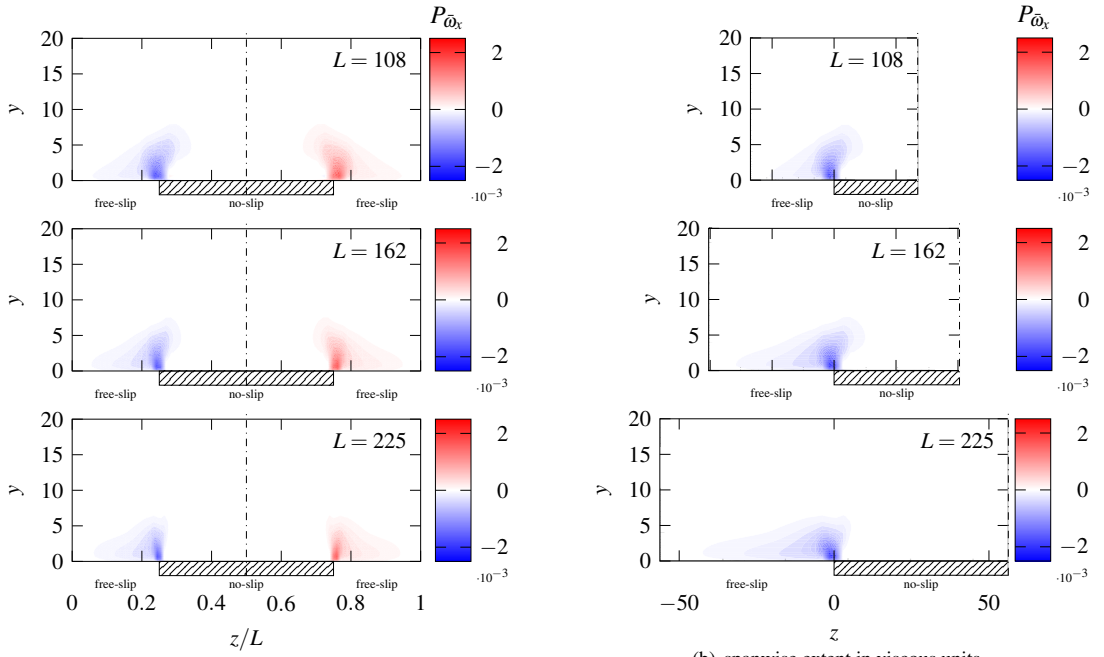

(a) wave-length normalized spanwise extent

(b) spanwise extent in viscous units

Figure 7. Vorticity production, $P_{\bar{\omega}_x}$, for $L = 108, 162, 225$ and $\Phi = 0.5$.

shear stress. This causes a formation of a vortex-pair located above the free-slip / no-slip edge with L-independent rotation direction inducing local motion towards the solid region. The vortex-pair interacts with the surrounding flow triggering a formation of additional tertiary structures in the outer parts of the flow. The organization of the structures depends on the wave-length as well as on the solid fraction of the introduced superhydrophobic surface. The spanwise and wall-normal vorticity production distribution extents remain very similar in viscous units around the free-slip / no-slip edges for different L, while the spanwise extent over the free-slip region scales with L. Comparison of the particular production terms unveils the fact that the vorticity production is dominated by two terms originating from the spanwise component of momentum equation. This is reasonable considering that the spanwise velocity component is significantly affected by the switch of the boundary conditions from free-slip to no-slip. The present knowledge provides useful information for modelling the secondary flow, and thus the resultant flow rate increase over SHS.

ACKNOWLEDGEMENTS

The authors greatly acknowledge the support by Karlsruhe House of Young Scientists (KHYS) through scholarship for research abroad and DFG project FR2823/2-1. This work was performed on the computational resource ForHLR Phase I funded by the Ministry of Science, Research and the Arts Baden-Württemberg and DFG ("Deutsche Forschungsgemeinschaft") within the framework program bwHPC.

REFERENCES

Cabral, B. & Leedom, L. C. 1993 Imaging vector fields using line integral convolution. In *Proceedings of the 20th Annual Conference on Computer Graphics and Interactive Techniques*, *SIGGRAPH '93* 20, pp. 263–270. New York, NY, USA: ACM.

Daniello, R., Waterhouse, N. & Rothstein, J. 2009 Drag reduction in turbulent flows over superhydrophobic surfaces. *Phys. Fluids* **21** (8), 085103.

Foss, J. F. 2004 Surface selections and topological constraint evaluations for flow field analyses. *Exp. Fluids* **37** (6), 883–898.

Fukagata, K., Kasagi, N. & Koumoutsakos, P. 2006 A theoretical prediction of friction drag reduction in turbulent flow by superhydrophobic surfaces. *Phys. Fluids* **18** (5), 051703–051703–4.

Goldstein, D. B. & Tuan, T.-C. 1998 Secondary flow induced by riblets. *J. Fluid Mech.* **363**, 115–151.

Martell, M. B., Perot, J. B. & Rothstein, J. P. 2009 Direct numerical simulations of turbulent flows over superhydrophobic surfaces. *J. Fluid Mech.* **620**, 31–41.

Min, T. & Kim, J. 2004 Effects of hydrophobic surface on skin-friction drag. *Phys. Fluids* **16** (7), L55.

Philip, J. 1972 Integral properties of flows satisfying mixed no-slip and no-shear conditions. *Zeitschrift für angewandte Mathematik und Physik ZAMP* **23** (6), 960–968.

Reynolds, W. C. & Hussain, A. K. M. F. 1972 The mechanics of an organized wave in turbulent shear flow. part 3. theoretical models and comparisons with experiments. *J. Fluid Mech.* **54** (02), 263–288.

Seo, J., García-Mayoral, R. & Mani, A. 2013 Pressure fluctuations in turbulent flows over superhydrophobic surfaces. In *Annual Research Briefs*, pp. 217–229. Center for Turbulence Research, Stanford University.

Türk, S., Daschiel, G., Stroh, A., Hasegawa, Y. & Frohnapfel, B. 2014 Turbulent flow over superhydrophobic surfaces with streamwise grooves. *J. Fluid Mech.* **747**, 186–217.